Physical properties, transmission and emission spectra of the WASP-19 planetary system from multi-colour photometry[★]

L. Mancini,[1,2]† S. Ciceri,[1] G. Chen,[1,3] J. Tregloan-Reed,[4] J. J. Fortney,[5]
J. Southworth,[4] T. G. Tan,[6] M. Burgdorf,[7] S. Calchi Novati,[2,8] M. Dominik,[9]‡
X.-S. Fang,[10] F. Finet,[11] T. Gerner,[12] S. Hardis,[13,14] T. C. Hinse,[15]
U. G. Jørgensen,[13,14] C. Liebig,[9] N. Nikolov,[1,16] D. Ricci,[11,17] S. Schäfer,[18]
F. Schönebeck,[12] J. Skottfelt,[13,14] O. Wertz,[11] K. A. Alsubai,[19] V. Bozza,[2,20]
P. Browne,[10] P. Dodds,[9] S.-H. Gu,[10,21] K. Harpsøe,[13,14] Th. Henning,[1]
M. Hundertmark,[9] J. Jessen-Hansen,[22] N. Kains,[23] E. Kerins,[24] H. Kjeldsen,[22]
M. N. Lund,[22] M. Lundkvist,[22] N. Madhusudhan,[25] M. Mathiasen,[13,14] M. T. Penny,[26]
S. Prof,[12] S. Rahvar,[27] K. Sahu,[28] G. Scarpetta,[2,8,20] C. Snodgrass[29] and J. Surdej[11]

[1]*Max Planck Institute for Astronomy, Königstuhl 17, D-69117 Heidelberg, Germany*
[2]*Department of Physics, University of Salerno, I-84084-Fisciano (SA), Italy*
[3]*Purple Mountain Observatory & Key Laboratory for Radio Astronomy, 2 West Beijing Road, Nanjing 210008, China*
[4]*Astrophysics Group, Keele University, Staffordshire ST5 5BG, UK*
[5]*Department of Astronomy & Astrophysics, University of California, Santa Cruz, CA 95064, USA*
[6]*Perth Exoplanet Survey Telescope, Perth, Australia*
[7]*HE Space Operations GmbH, Flughafenallee 24, D-28199 Bremen, Germany*
[8]*Istituto Internazionale per gli Alti Studi Scientifici (IIASS), I-84019 Vietri Sul Mare (SA), Italy*
[9]*SUPA, University of St Andrews, School of Physics & Astronomy, North Haugh, St Andrews KY16 9SS, UK*
[10]*National Astronomical Observatories/Yunnan Observatory, Chinese Academy of Sciences, Kunming 650011, China*
[11]*Institut d'Astrophysique et de Géophysique, Université de Liège, B-4000 Liège, Belgium*
[12]*Zentrum für Astronomie, Universität Heidelberg, Mönchhofstraße 12-14, D-69120 Heidelberg, Germany*
[13]*Niels Bohr Institute, University of Copenhagen, Juliane Maries vej 30, DK-2100 Copenhagen Ø, Denmark*
[14]*Centre for Star and Planet Formation, Geological Museum, Øster Voldgade 5-7, DK-1350 Copenhagen, Denmark*
[15]*Korea Astronomy and Space Science Institute, Daejeon 305-348, Republic of Korea*
[16]*Astrophysics Group, University of Exeter, Stocker Road, Exeter EX4 4QL, UK*
[17]*Instituto de Astronomía – UNAM, Km 103 Carretera Tijuana Ensenada, 422860, Ensenada (Baja Cfa), Mexico*
[18]*Institut für Astrophysik, Georg-August-Universität Göttingen, Friedrich-Hund-Platz 1, D-37077 Göttingen, Germany*
[19]*Qatar Foundation, PO Box 5825, Doha, Qatar*
[20]*Istituto Nazionale di Fisica Nucleare, Sezione di Napoli, Napoli, Italy*
[21]*Key Laboratory for the Structure and Evolution of Celestial Objects, Chinese Academy of Sciences, Kunming 650011, China*
[22]*Stellar Astrophysics Centre, Department of Physics and Astronomy, Aarhus University, Ny Munkegade 120, DK-8000 Aarhus C, Denmark*
[23]*European Southern Observatory, Karl-Schwarzschild-Straße 2, D-85748 Garching bei München, Germany*
[24]*Jodrell Bank Centre for Astrophysics, University of Manchester, Oxford Road, Manchester M13 9PL, UK*
[25]*Department of Physics and Department of Astronomy, Yale University, New Haven, CT 06511, USA*
[26]*Department of Astronomy, Ohio State University, 140 W. 18th Ave., Columbus, OH 43210, USA*
[27]*Department of Physics, Sharif University of Technology, P. O. Box 11155-9161 Tehran, Iran*
[28]*Space Telescope Science Institute, 3700 San Martin Drive, Baltimore, MD 21218, USA*
[29]*Max-Planck-Institute for Solar system Research, Max-Planck Str. 2, D-37191 Katlenburg-Lindau, Germany*

ABSTRACT

We present new ground-based, multi-colour, broad-band photometric measurements of the physical parameters, transmission and emission spectra of the transiting extrasolar planet WASP-19b. The measurements are based on observations of eight transits and four occultations

[★] Based on data collected with the Gamma Ray Burst Optical and Near-Infrared Detector (GROND) at the MPG/ESO 2.2 m telescope and by MiNDSTEp with the Danish 1.54-m telescope at the ESO Observatory in La Silla.
† E-mail: mancini@mpia-hd.mpg.de
‡ Royal Society University Research Fellow.

through a Gunn i filter using the 1.54-m Danish Telescope, 14 transits through an R_c filter at the Perth Exoplanet Survey Telescope (PEST) observatory and one transit observed simultaneously through four optical (Sloan g', r', i', z') and three near-infrared (J, H, K) filters, using the Gamma Ray Burst Optical and Near-Infrared Detector (GROND) instrument on the MPG/ESO 2.2-m telescope. The GROND optical light curves have a point-to-point scatter around the best-fitting model between 0.52 and 0.65 mmag rms. We use these new data to measure refined physical parameters for the system. We find the planet to be more bloated ($R_b = 1.410 \pm 0.017 R_{Jup}$; $M_b = 1.139 \pm 0.030 M_{Jup}$) and the system to be twice as old as initially thought. We also used published and archived data sets to study the transit timings, which do not depart from a linear ephemeris. We detected an anomaly in the GROND transit light curve which is compatible with a spot on the photosphere of the parent star. The starspot position, size, spot contrast and temperature were established. Using our new and published measurements, we assembled the planet's transmission spectrum over the 370–2350 nm wavelength range and its emission spectrum over the 750–8000 nm range. By comparing these data to theoretical models we investigated the theoretically predicted variation of the apparent radius of WASP-19b as a function of wavelength and studied the composition and thermal structure of its atmosphere. We conclude that: (*i*) there is no evidence for strong optical absorbers at low pressure, supporting the common idea that the planet's atmosphere lacks a dayside inversion; (*ii*) the temperature of the planet is not homogenized, because the high warming of its dayside causes the planet to be more efficient in re-radiating than redistributing energy to the night side; (*iii*) the planet seems to be outside of any current classification scheme.

1 INTRODUCTION

The study of extrasolar planets is now decisively in a phase of rapid expansion and extraordinary discoveries. More than 850 planets have been detected orbiting around stars other than our Sun. They show a wide range of characteristics in terms of mass, radius, density, temperature, and distance from their parent stars. Among these planets, those that transit are prime sources of information on the physical properties and atmospheric characteristics of planets. Such information is precious as we seek to establish reliable theories of their formation and evolution. For these reasons, transiting extrasolar planets (TEPs) are the most important and interesting ones to study in detail.

In this paper we focus on WASP-19b (Hebb et al. 2010), which is an extremely short period TEP moving on a circular orbit (Lendl et al. 2012; Anderson et al. 2013) around a G8 V star every 0.79 d. Hebb et al. (2010) measured its mass to be $1.15 \pm 0.08 M_{Jup}$ and its radius to be $1.31 \pm 0.06 R_{Jup}$, which together imply that WASP-19b is a slightly bloated hot Jupiter. Its orbital semimajor axis, $\sim$0.016 au, places it in the class of highly irradiated planets. The star–planet separation is equivalent to only 1.2 times the Roche tidal radius and suggests that WASP-19b has spiralled inward to its current location likely via the Kozai mechanism or tidal dissipation (Hellier et al. 2011). Its position in the planetary radius-separation diagram is shown in Fig. 1.

Radial velocity (RV) follow-up observations of WASP-19 have been obtained using the HARPS spectrograph to successfully detect the Rossiter–McLaughlin effect. This resulted in a measurement of the angle between the planet's orbit and the sky-projected stellar rotation axis of $\lambda = 4°\!\!.6 \pm 5°\!\!.2$, implying an aligned orbit for WASP-19b (Hellier et al. 2011). Both photometric and spectroscopic data show modulations compatible with starspot activity on the parent star (Hebb et al. 2010; Hellier et al. 2011; Abe et al. 2013). This

activity has been directly observed by Tregloan-Reed, Southworth & Tappert (2013), who reported a starspot in two consecutive planetary transits of WASP-19b. They used it to obtain a better constraint on λ ($1°\!\!.0 \pm 1°\!\!.2$) and measure the star's rotation period and velocity (11.76 ± 0.09 d and 3.88 ± 0.15 km s^{-1}, respectively).

Occultations (secondary eclipses) of WASP-19b, observed in several near-infrared (NIR) (Gibson et al. 2010; Anderson et al. 2010) and infrared (IR) (Anderson et al. 2013) bands with the VLT and *Spitzer*, respectively, suggest that the dayside atmosphere of WASP-19b lacks a temperature inversion. This picture does not support the 'TiO/VO hypothesis' of Fortney et al. (2008), and is instead in favour of a monotonically decreasing atmospheric temperature with pressure. Evidence of WASP-19b occultations from the ground at optical wavelengths have also been presented by Burton et al. (2012), Lendl et al. (2012) and Abe et al. (2013), extending our knowledge of the thermal emission of WASP-19b. Recently, time series spectroscopy in nine channels (1250–2350 nm) were performed by Bean et al. (2013) on the Magellan II telescope during two transits and two occultations of WASP-19. These observations again question a thermal inversion and favour the presence of HCN and H_2O molecules. The whole set of data occultation slightly supports a carbon-rich instead of an oxygen-rich planetary atmosphere (Madhusudhan 2012).

In this paper we present observations of eight transits and four occultations in the WASP-19 system obtained with the 1.54-m Danish Telescope, one transit observed simultaneously in four optical and three NIR passbands using Gamma Ray Burst Optical and Near-Infrared Detector (GROND) on the MPG/ESO 2.2-m telescope, and 14 transits observed with the 0.3-m Perth Exoplanet Survey Telescope (PEST). These new data allow us to study the physical properties of the whole system, and the transmission and emission spectra of the planet. The differential photometry will be made available at the CDS.
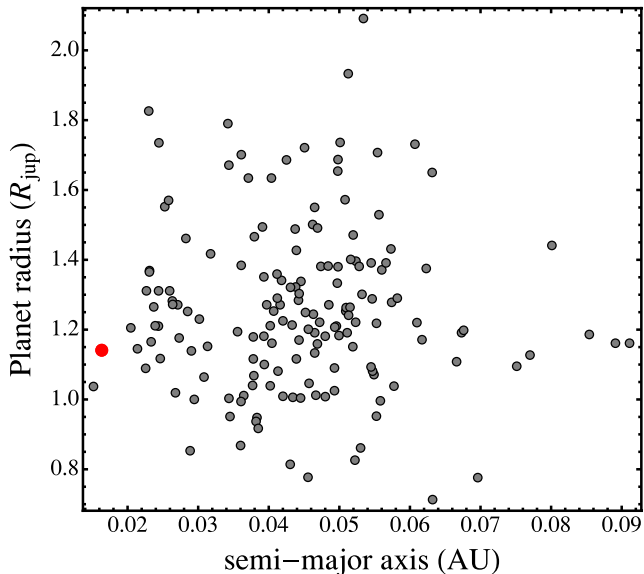
Figure 1. Plot of planet radius versus semimajor axis for the known TEPs with mass $>0.1\,M_{\rm jup}$ and $P_{\rm orb} < 10$ d. The red point represents WASP-19b. The error bars of the planets have been suppressed for clarity. Data taken from TEP Catalogue, available at http://www.astro.keele.ac.uk/jkt/tepcat/.

Our paper is structured as follows. In Section 2 we describe the observations and data reduction methodology. In Section 3 we analyse the transit light curves to refine the orbital ephemerides, obtain the photometric parameters of the WASP-19 system, and characterize the starspot detected in the GROND light curves. The revision of the physical properties of the system is presented in Section 4, while Section 5 is dedicated to the study of the variation of the planetary radius as function of wavelength. The analysis of the occultation light curves is described in Section 6. Our conclusions are summarized in Section 7.

2 OBSERVATIONS AND DATA REDUCTION

2.1 Transits

One partial transit and seven full transits of WASP-19 were observed using the DFOSC imager mounted on the 1.54-m Danish Telescope at La Silla during the MiNDSTEp campaigns in 2010 and 2011 (Dominik et al. 2010). The instrument has a field of view (FOV) of 13.7×13.7 arcmin^2 and a plate scale of 0.39 arcsec pixel^{-1}. All the observations were performed through a Gunn i filter and using the *defocussing* method (Southworth et al. 2009a,b). The telescope was autoguided and the CCD was windowed to reduce the readout time. Night logs are reported in Table 1. The data were analysed using the IDL[1] pipeline from Southworth et al. (2009a), which uses the IDL implementation of DAOPHOT (Stetson 1987). The images were debiased and flat-fielded using standard methods, then subjected to aperture photometry using the APER[2] task and an optimal ensemble of comparison stars. Pointing variations were followed by cross-correlating each image against a reference image. The shape of the

light curves is very insensitive to the aperture sizes, so we chose those which yielded the lowest scatter. The absolute values of the experimental errors calculated by APER are often underestimated, so we enlarged the error bars for each transit to give a reduced χ^2 of $\chi_\nu^2 = 1$. We then further inflated the error bars using the β approach (e.g. Gillon et al. 2006; Winn et al. 2008; Gibson et al. 2008) to account for any correlated noise. The eight light curves are plotted in Fig. 2.

One transit of WASP-19 was observed on 2012 April 15, with the GROND instrument mounted on the MPG[3]/ESO 2.2 m telescope at ESO La Silla, Chile. GROND is an imaging system capable of simultaneous photometric observations in four optical (similar to Sloan g', r', i', z') and three NIR (J, H, K) passbands (Greiner et al. 2008). Each of the four optical channels is equipped with a back-illuminated 2048×2048 E2V CCD, with a FOV of $5.4' \times 5.4'$ at a scale of 0.158 arcsec pixel^{-1}. The three NIR channels use 1024×1024 Rockwell HAWAII-1 arrays with an FOV of 10×10 arcmin^2 at 0.6 arcsec pixel^{-1}. The accuracy of the GROND photometry was recently analysed by Pierini et al. (2012), who computed the uncertainty of the total photometry in each of the broad-bands as a function of the total magnitude of sources with different brightness. From this analysis it emerges that for bright stars (<15 mag in each passband) the uncertainty in the optical bands is <0.01 mag, while that in the NIR bands is ≥ 0.02 mag, the K band giving the worst results. In order to improve the accuracy, we used the telescope defocussing technique during the follow-up of the planetary transit of WASP-19, which indeed provided a better photometry (by a factor $\sim$3) in comparison to previous uses of this instrument (see Nikolov et al. 2012; Harpsøe et al. 2013; Mancini et al. 2013b).

The optical data were reduced as for the Danish Telescope. The NIR data were calibrated by performing dark subtraction, readout pattern removal and flat division on the raw science images. Both the dark and flat master frames were created through median-combining a stack of individual measurements, for which the twilight sky flats were adopted. We also removed the odd–even readout pattern (along the x-axis) before the flat correction by shifting the count level of each column to a common overall level. After the calibration, we obtained light curves using an aperture photometry routine again based on the IDL/DAOPHOT package. To determine the centroids of WASP-19 and its comparison stars, we smoothed the defocused images into a lower resolution and fitted Gaussians to the marginal x, y distributions. We also recorded the full-width at half-maximum (FWHM) by fitting the wing of original point spread function, the central region of which has been masked out. We carefully chose the comparison stars that were of similar brightness and well within the saturation limit. The companions close to our chosen stars were masked out in case they contaminated the photometry. Fluxes of these comparison stars were weighted-averaged together after self-normalization, and divided from that of WASP-19. We also experimented with a set of aperture and sky annulus sizes, and adopted that which yielded the light curve with least scatter. The final light curves were decorrelated with star position, FWHM, time and airmass. Uncertainties were treated as for the optical case. Optical and NIR GROND light curves are shown in Fig. 3. A clear anomaly is visible in the four optical bands close to the midpoint of the transit.

Fourteen transits of WASP-19 were observed between 2011 February and November at the PEST observatory, which consists

---

[1] The acronym IDL stands for Interactive Data Language and is a trademark of ITT Visual Information Solutions. For further details see http://www.ittvis.com/ProductServices/IDL.aspx.
[2] APER is part of the ASTROLIB subroutine library distributed by NASA. For further details see http://idlastro.gsfc.nasa.gov.

[3] Max Planck Gesellschaft.

Table 1. Details of the transit observations presented in this work. N_{obs} is the number of observations, T_{exp} is the exposure time, T_{obs} is the observational cadence and 'Moon illum.' is the fractional illumination of the Moon at the midpoint of the transit.

Transit	Date of first obs	Start time (UT)	End time (UT)	N_{obs}	T_{exp} (s)	T_{obs} (s)	Filter	Airmass	Moon illum.	Aperture radii (px)	Scatter (mmag)
DFOSC	2010 05 18	01:04	04:37	95	100	125	Gunn i	$1.15 \rightarrow 2.49$	0.19	17, 40, 65	0.83
DFOSC	2010 06 02	00:20	03:22	75	90	115	Gunn i	$1.19 \rightarrow 2.27$	0.76	18, 35, 65	1.33
DFOSC	2010 06 05	23:28	03:24	80	120	155	Gunn i	$1.12 \rightarrow 2.53$	0.39	19, 40, 65	0.88
DFOSC	2010 06 20	23:08	02:18	92	90	115	Gunn i	$1.19 \rightarrow 2.45$	0.70	16, 40, 65	1.92
DFOSC	2011 05 08	00:04	05:12	121	120	155	Gunn i	$1.05 \rightarrow 2.43$	0.22	16, 35, 45	1.60
DFOSC	2011 05 11	23:16	03:31	121	90	115	Gunn i	$1.05 \rightarrow 1.65$	0.64	17, 35, 65	0.80
DFOSC	2011 05 22	23:47	03:53	71	150	185	Gunn i	$1.09 \rightarrow 2.19$	0.67	24, 45, 75	1.43
DFOSC	2011 05 26	23:03	02:38	82	120	155	Gunn i	$1.05 \rightarrow 1.62$	0.29	19, 35, 65	0.99
GROND	2012 04 15	23:17	03:02	114	90	120	Gunn g'	$1.08 \rightarrow 1.00 \rightarrow 1.15$	0.23	33, 55, 85	0.59
GROND	2012 04 15	23:17	03:02	114	90	120	Gunn r'	$1.08 \rightarrow 1.00 \rightarrow 1.15$	0.23	33, 55, 80	0.52
GROND	2012 04 15	23:17	03:02	114	90	120	Gunn i'	$1.08 \rightarrow 1.00 \rightarrow 1.15$	0.23	36, 55, 80	0.52
GROND	2012 04 15	23:17	03:02	114	90	120	Gunn z'	$1.08 \rightarrow 1.00 \rightarrow 1.15$	0.23	32, 55, 80	0.65
GROND	2012 04 15	23:17	03:02	339	10	50	J	$1.08 \rightarrow 1.00 \rightarrow 1.15$	0.23	6.5, 10.5, 21	1.59
GROND	2012 04 15	23:17	03:02	339	10	50	H	$1.08 \rightarrow 1.00 \rightarrow 1.15$	0.23	5, 12, 22	2.22
GROND	2012 04 15	23:17	03:02	339	10	50	K	$1.08 \rightarrow 1.00 \rightarrow 1.15$	0.23	7, 11, 19	2.82

of a 30-cm Meade LX200 SCT f/10 telescope, with a focal reducer converting this to f/5, and equipped with an SBIG ST-8XME camera. The image scale is 1.2 arcsec pixel^{-1} and the FOV is 31×21 arcmin^2. This backyard observatory is located in a suburb of the city of Perth (Western Australia). The transit observations were performed using an Astrodon R_c filter and the telescope was autoguided. The images were reduced and the photometry performed using the software package C-MUNIPACK. Raw sky-flat frames were bias-subtracted and then median combined to obtain a master flat frame. For each data set, sky flats from the dusk preceding, or dawn succeeding the observations were used when possible, otherwise the latest available master flat was used. The science frames were dark subtracted and flat-field corrected and then subjected to aperture photometry. Finally, all the data sets were phased-binned and the corresponding light curve is plotted in Fig. 4.

2.2 Occultations

Four occultations of WASP-19 were followed through a Gunn i filter using the Danish Telescope and DFOSC. One was observed in 2010 May and the others between 2011 May and June (Table 2). The images were calibrated in the standard way, including bias subtraction and flat division. We created master bias and master skyflat frames through median combination of a set of individual files, and then corrected the bias and flat-field from the science images. We performed aperture photometry on the calibrated science images employing the IDL/DAOPHOT routines. Since the telescope was heavily defocused, to find the centroids of stars, we convolved the science images with a Gaussian kernel so that the doughnut-shaped point spread functions became approximately Gaussian. The locations of WASP-19 as well as an ensemble of nearby comparison stars of similar brightness were determined by employing IDL/FIND on these convolved images. We placed 30 apertures on each star in steps of 1 pixel. 10 annuli for each aperture were tried in steps of 2 pixels. We normalized the light curve of each star by dividing their out-of-eclipse flux level individually. We checked each star to remove the ones that were saturated and carefully chose the ensemble with a similar light curve shape to WASP-19. The chosen ensemble was weight-combined as the composite reference light curve, which was then used to normalize the WASP-19 light curve. These normalized light curves were modelled, and the one with the

lowest standard deviation of the residuals was chosen as the optimal light curve. The aperture settings are listed in Table 2 together with the details of the observations. The four light curves are shown in Fig. 5.

3 LIGHT-CURVE ANALYSIS

Fig. 3 shows the multi-band GROND light curves of one transit. There is an anomaly near to the midpoint of the transit which could not be removed by choosing different comparison stars. The light curves are shown superposed in Fig. 6 to allow comparison of the transit depth and starspot anomaly in each passband. Following Tregloan-Reed et al. (2013), we interpret this anomaly as the consequence of a dark starspot on the stellar photosphere. These light curves were analysed with a dedicated code and discussed in Section 3.3. We do not see any colour-depending variation in the transit depth similar to that detected by Lendl et al. (2012) in their simultaneous observation of a transit of WASP-19 with two different telescopes and optical broad-band filters.

The other WASP-19 transit light curves presented in Section 2.1 were analysed using the JKTEBOP[4] code (Southworth, Maxted & Smalley 2004). The main fitted parameters were the orbital inclination, i, the transit midpoint, T_0, and the sum and ratio of the fractional radii of the star and planet, $r_A + r_b$ and $k = r_b/r_A$, where $r_A = R_A/a$ and $r_b = R_b/a$, a is the orbital semimajor axis, and R_A and R_b are the absolute radii of the star and the planet, respectively. The occultation light curves were analysed with a different procedure (see Section 6). The orbital eccentricity was fixed to zero (Anderson et al. 2013) throughout the analysis.

3.1 Orbital period determination

We used our photometric data to refine the orbital period of WASP-19b. The transit time for each of our data sets was obtained by fitting them with JKTEBOP, and uncertainties were estimated by Monte Carlo simulations. To these we added three timings from high-precision light curves obtained by Tregloan-Reed et al. (2013), 14 timings

---

[4] JKTEBOP is written in FORTRAN77 and the source code is available at: www.astro.keele.ac.uk/jkt/codes/jktebop.html
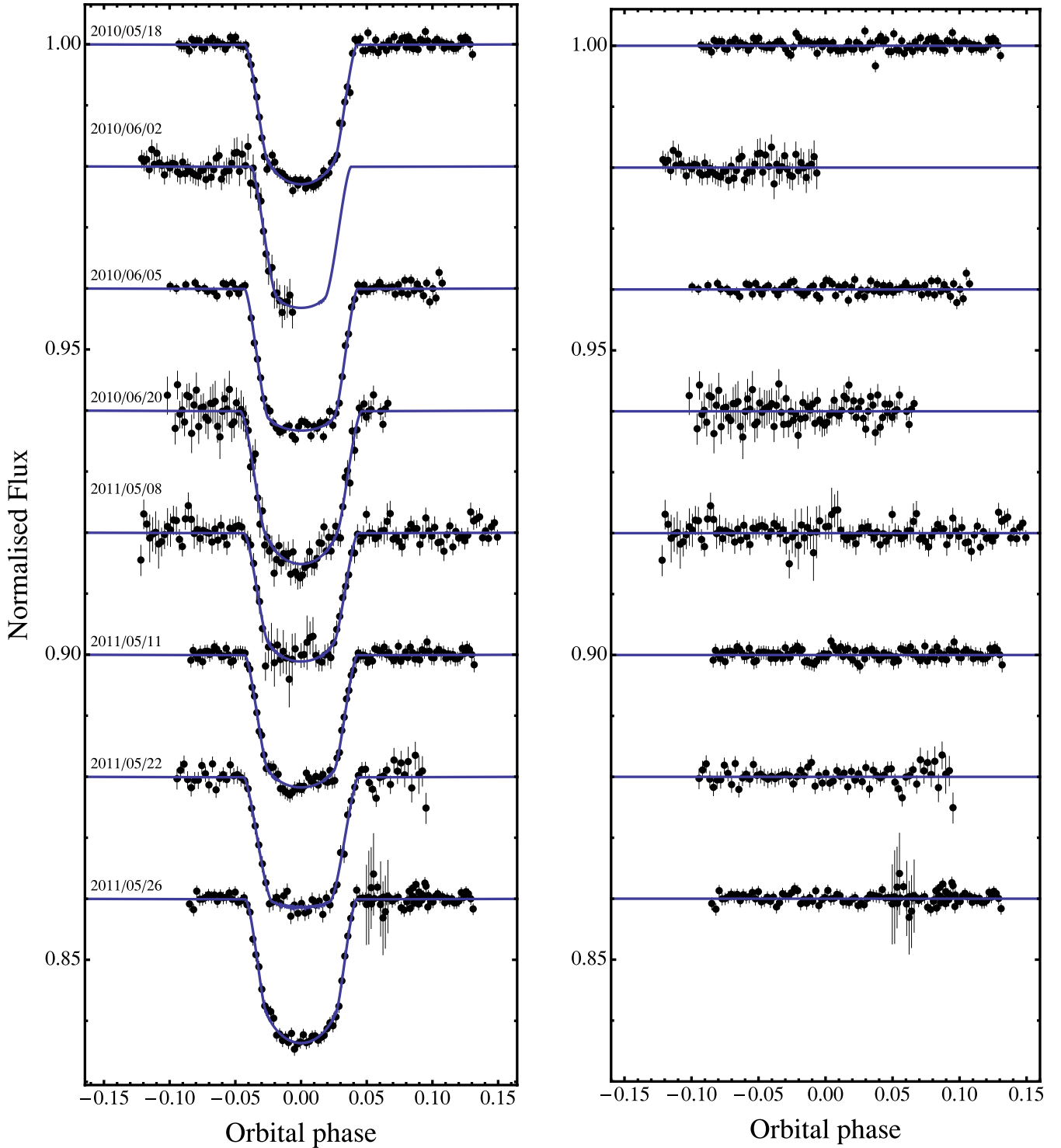
Figure 2. Light curves of eight transits observed with DFOSC through a Gunn *i* filter (left panel), plotted in date order. The JKTEBOP best fit is also shown for each data set, and the residuals of each fit are plotted in the right-hand panel.

from Lendl et al. (2012), five from literature sources and another seven measured by amateur astronomers and available on the ETD[5] website, for a total of 54 times of mid-transit. The ETD light curves were included only if they had complete coverage of the transit and a

Data Quality index ≤3. We recalculated the timing from Dragomir et al. (2011) by fitting this light curve with JKTEBOP (Fig. 4). All timings were placed on BJD(TDB) time system and are summarized in Table 3. The resulting measurements of transit midpoints were fitted with a straight line to obtain a final orbital ephemeris:

[5] The Exoplanet Transit Database (ETD) website can be found at http://var2.astro.cz/ETD

$$T_0 = \text{BJD(TDB)}2\,45\,4775.337\,45(35) + 0.788\,8396(10)\,E,$$
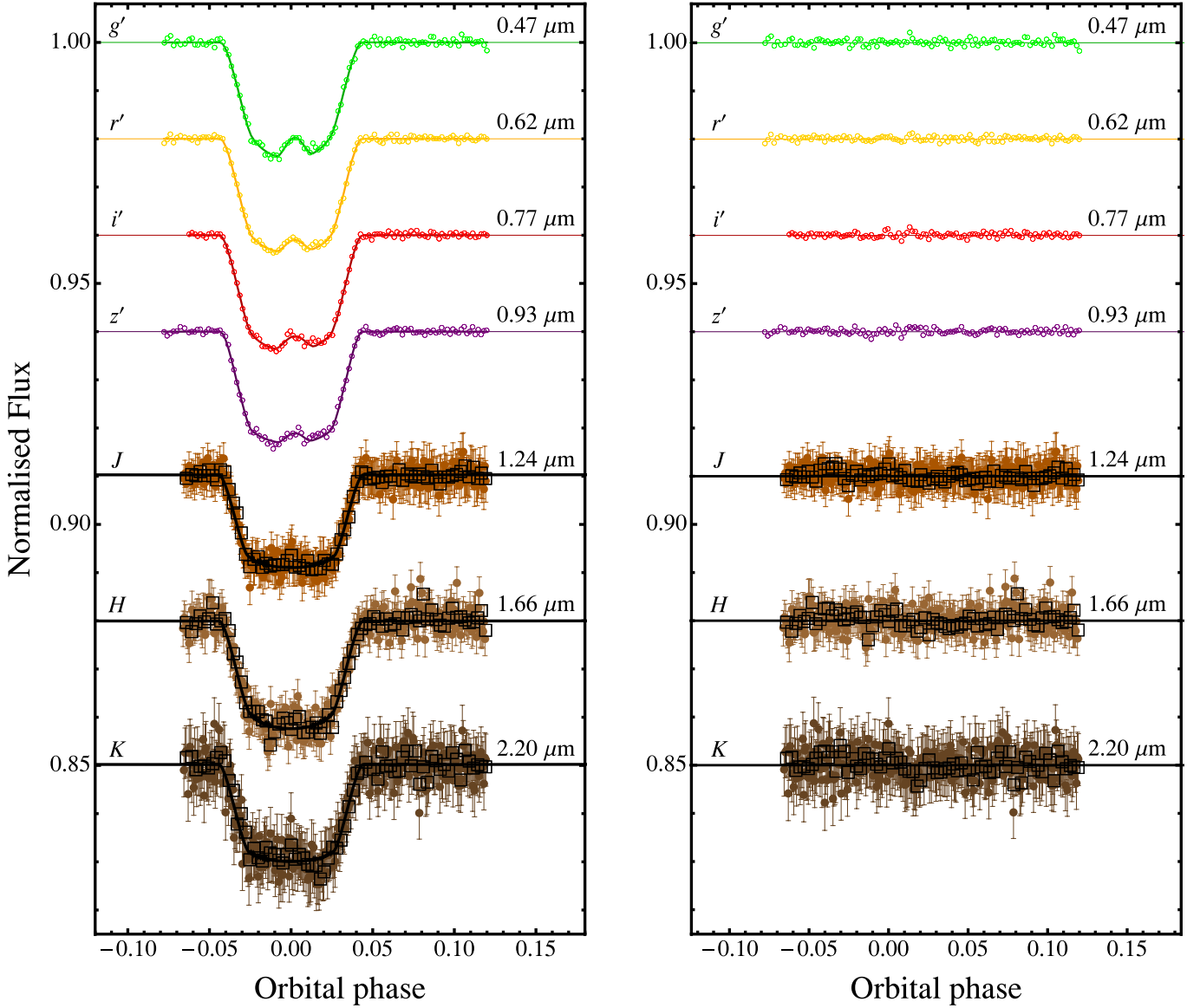
Figure 3. Left-hand panel: simultaneous optical and NIR light curves of one transit event of WASP-19b observed with GROND. Black empty squares show the three NIR light curves binned using a bin size of 0.002 phase units. The PRISM+GEMC best fits are shown as solid lines for each optical data set, while for the NIR ones the best fits were found with JKTEBOP. The passbands are labelled on the left of the figure, and their central wavelengths are given on the right. The error bars of the optical data have been suppressed for clarity. The bump observed in the optical light curves, roughly at the mid-transit time, is interpreted as the occultation of a starspot by the planet (see Section 3.3). Right-hand panel: the residuals of each fit.

where E is the number of orbital cycles after the reference epoch, which we take to be the midpoint of the first transit observed by Hebb et al. (2010), and quantities in brackets denote the uncertainty in the final digit of the preceding number. The fit has $\chi_\nu^2 = 1.98$, which is significantly greater than unity. The uncertainties in the ephemeris given above have been increased to account for this. The large χ_ν^2 implies that the error bars in the various T_0 measurements are too small. A plot of the residuals around the fit is shown in Fig. 7 and does not indicate any clear systematic deviation from the predicted transit times. Based on our experience with a similar situation in previous studies (e.g. Southworth et al. 2012a,b; Mancini et al. 2013a), we conservatively do not interpret the large χ_ν^2 as indicating transit timing variations.

3.2 Optical light-curve modelling

The light curves from DFOSC were individually analysed, while the PEST ones were normalized to zero magnitude, phase-binned and fitted with JKTEBOP. We used a quadratic law to model the limb darkening (LD) of the star. For each instrument, the two LD coefficients were selected considering the filter used and their theoretically predicted values from Claret (2004). The atmospheric parameters of the star adopted to derive the LD coefficients are shown in Table 4. The linear LD coefficients were fitted, whereas the non-linear ones were fixed but perturbed during the process of error estimating. Uncertainties in the fitted parameters from each solution were calculated from 3000 Monte Carlo simulations and by a residual-permutation algorithm (Southworth 2008). The larger of the two possible error
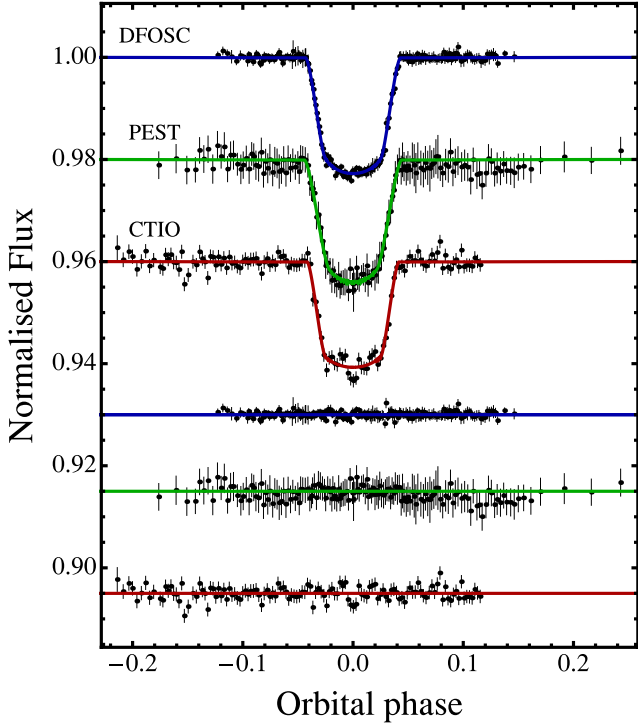
Figure 4. Top: transit light curve of WASP-19 obtained by phase-binning (bin size 0.01) all the DFOSC light curves shown in Fig. 2. Middle: phased-binned light curve derived from the 14 transits observed with PEST. Bottom: light curve one transit observed by Dragomir et al. (2011) using the CTIO 1 m telescope and a Cousins *R* filter. The JKTEBOP best fit is also shown for each data set, and the residuals of each fit are plotted near the base of the figure.

bars was retained in each case. The light curves and their best-fitting models are shown in Fig. 2 for the DFOSC light curves and in Fig. 4 for the PEST data. An investigation of the residuals in the right-hand panel of Fig. 2 suggests that they are probably contaminated by systematic noise. Another explanation is related to the starspot activity in the photosphere of the parent star. This possibility is discussed in Section 3.3. Finally, the DFOSC light curves were combined by phase, binned and refitted with JKTEBOP. The final light curve has a scatter around the best-fitting model of 0.58 mmag.

The parameters of each fit with their uncertainties are reported in Table 5. They were combined with those coming from the analysis of the GROND optical data (see Section 3.3), whereas the GROND NIR light curves were ignored at this point due to their much larger scatter (Fig. 3). The final photometric parameters are the weighted mean of all the results presented in Table 5. Values obtained by other authors are also reported for comparison.

3.3 Starspot modelling

We modelled the GROND transit light curves of WASP-19 with the PRISM[6] and GEMC[7] codes (Tregloan-Reed et al. 2013). The first code models a planetary transit over a spotted star, while the latter one is an optimization algorithm for finding the global best fit and

---

[6] Planetary Retrospective Integrated Star-spot Model.
[7] Genetic Evolution Markov Chain.

associated uncertainties. Using these codes, it is then possible not only to determine k, $r_A + r_b$, i, T_0 and the LD coefficients, but also the parameters of the starspot. The starspot parameters are the projected longitude and the latitude of its centre (θ and ϕ), its angular radius r_{spot} and its contrast ρ_{spot}, the latter being the ratio of the surface brightness of the starspot to that of the surrounding photosphere.

Since the codes are not able to simultaneously fit the four GROND data sets, we performed a two-step analysis. First, we modelled all the GROND data sets separately and determined the photometric parameters which we reported in Table 5. These were used to revise the physical properties of the system (see Section 4). In the second step, we combined the four light curves into a single data set by taking the mean value at each point from the four optical bands at that point and we fitted the corresponding light curve. In this way we found a common value for T_0, i, θ and ϕ. The values of the latter two quantities are $\theta = 3°.36 \pm 0°.08$ and $\phi = 59°.98 \pm 0°.80$. Finally, we refitted each light curve separately, this time fixing θ and ϕ to the values found in the combined fit, and deriving r_{spot} and ρ_{spot} in each band (Table 6).

The final value for the spot angular radius comes from the weighted mean of the results in each band and is $r_{spot} = 9°.46 \pm 0°.26$. This translates to a radius of $116\,900 \pm 3220$ km, which is equivalent to a size of 2.7 per cent of the stellar disc and is ~68 460 km smaller than the starspot found by Tregloan-Reed et al. (2013). The sizes of starspots are most often estimated through Doppler-imaging techniques (e.g. Collier Cameron 1992; Vogt et al. 1999), which are unable to measure starspots with a size less than 0.1 per cent of a stellar hemisphere (Strassmeier 2009). However, our measurement is similar to those found for other G-type stars and is in good agreement with the sizes of common sunspots.

It is also interesting to study how starspot contrast changes with passband. Starspots are expected to be darker in the ultraviolet (UV) than in the IR. In our case, as can be seen from Table 6, moving from g' to z', the starspot becomes brighter (note that the values for i' and z' are well within 1σ). Modelling both the photosphere and the starspot as black bodies (Rabus et al. 2009; Sanchis-Ojeda & Winn 2011) and using equation (1) of Silva (2003) and $T_{eff} = 5460 \pm 90$ (Doyle et al. 2013), we found the temperature of the starspot in each band: $T_{spot,g} = 4595 \pm 118$ K, $T_{spot,r} = 4864 \pm 96$ K, $T_{spot,i} = 4842 \pm 81$ K and $T_{spot,z} = 4698 \pm 112$ K. The weighted mean is $T_{spot} = 4777 \pm 50$ K, and is consistent with what has been observed for other stars (see Fig. 8) and for the case of the TrES-1 (Rabus et al. 2009), HD189733 (Sing et al. 2011) and HATS-2 (Mohler-Fischer et al. 2013).

Finally, we investigated whether the systematic residuals from fitting the transit DFOSC light curves can be attributed to starspots. We selected one of the best DFOSC light curves, that of 2011/05/11, and refitted it using PRISM+GEMC. The fit includes a starspot just after mid-transit with starspot parameters in reasonable agreement with that of the starspot detected in the GROND data (this work) and in the NTT data (Tregloan-Reed et al. 2013). The best fit is visible in Fig. 9 and the fitted parameters are shown in Table 7, together with those obtained without considering the starspot. The presence of the starspot cannot be confirmed because the amplitude of the anomaly is similar to the scatter of the data points.

4 PHYSICAL PROPERTIES

We measured the physical properties of the WASP-19 system using the *Homogeneous Studies* methodology (see Southworth 2012;

**Table 2.** Details of the occultation observations presented in this work. See Table 2 for the explanation of N_{obs}, T_{exp}, T_{obs} and Moon illum. $\sigma_{300\,s}$ is the standard deviation of residuals binned every 5 minute, and β is the ratio between the noise levels due to Poisson noise and combined Poisson and red noise.

Occultation	Date of first obs	Start time (UT)	End time (UT)	N_{obs}	T_{exp} (s)	T_{obs} (s)	Filter	Airmass	Moon illum.	Aperture radii (px)	$\sigma_{300\,s}$ (ppm)	β
DFOSC	2010 05 23	23:03	03:01	91	120	155	Gunn i	1.05 → 1.73	0.60	18, 24, 32	547	1.00
DFOSC	2011 05 13	22:59	02:34	100	90	115	Gunn i	1.04 → 1.35	0.84	22, 32, 39	420	1.16
DFOSC	2011 05 24	23:09	03:28	94	120	155	Gunn i	1.03 → 2.01	0.48	21, 27, 35	537	1.00
DFOSC	2011 06 08	23:23	03:11	84	120	115	Gunn i	1.13 → 2.44	0.50	18, 24, 32	816	1.12
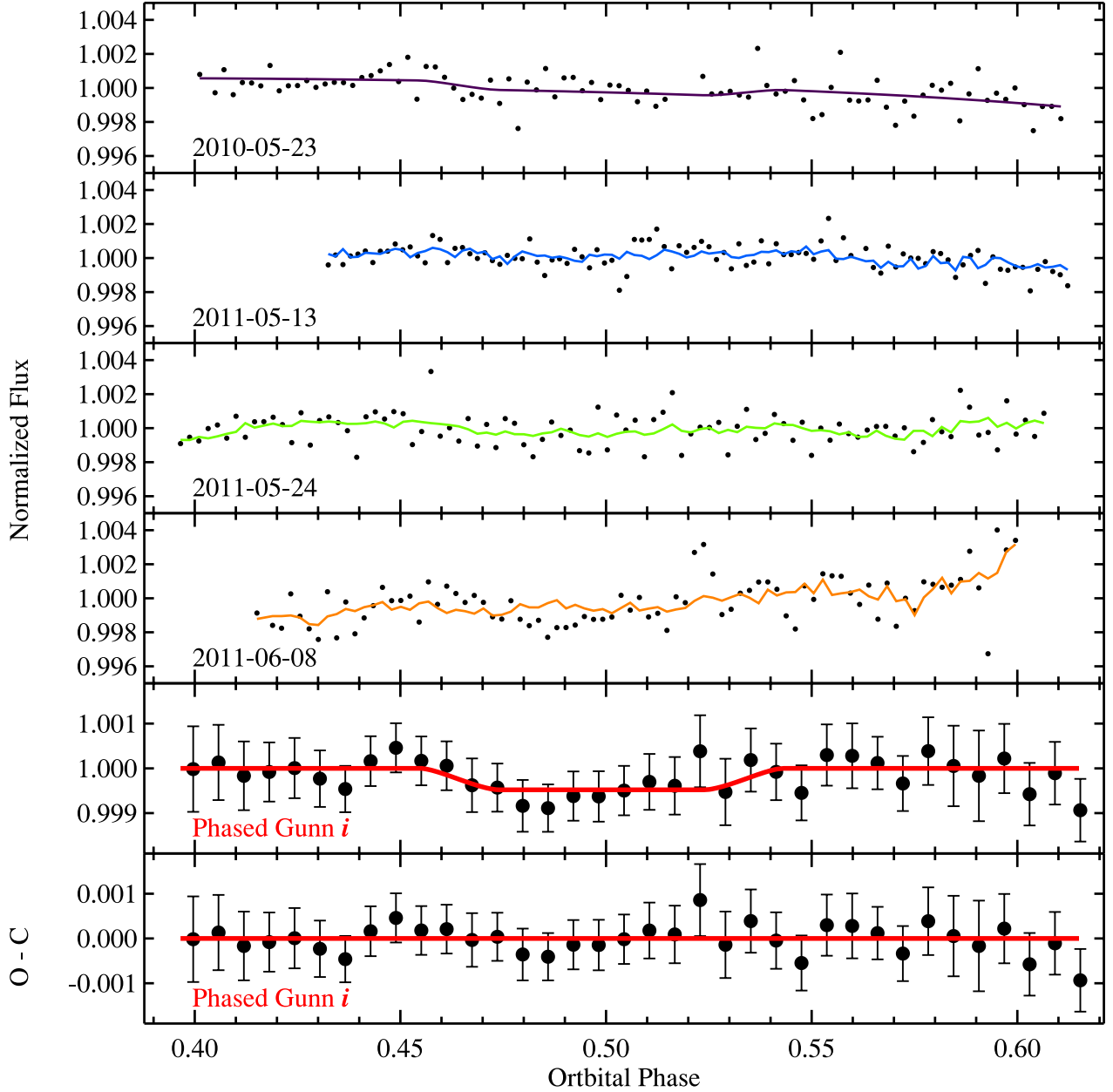
Figure 5. Occultation light curves observed with DFOSC in Gunn i. Panels 1 to 4: the raw light curves of four individual nights, overplotted with the best-fitting model. Panel 5: the phase-folded occultation light curve after correction for baseline slope and binned in every 7 minute. Panel 6: corresponding O–C residuals.
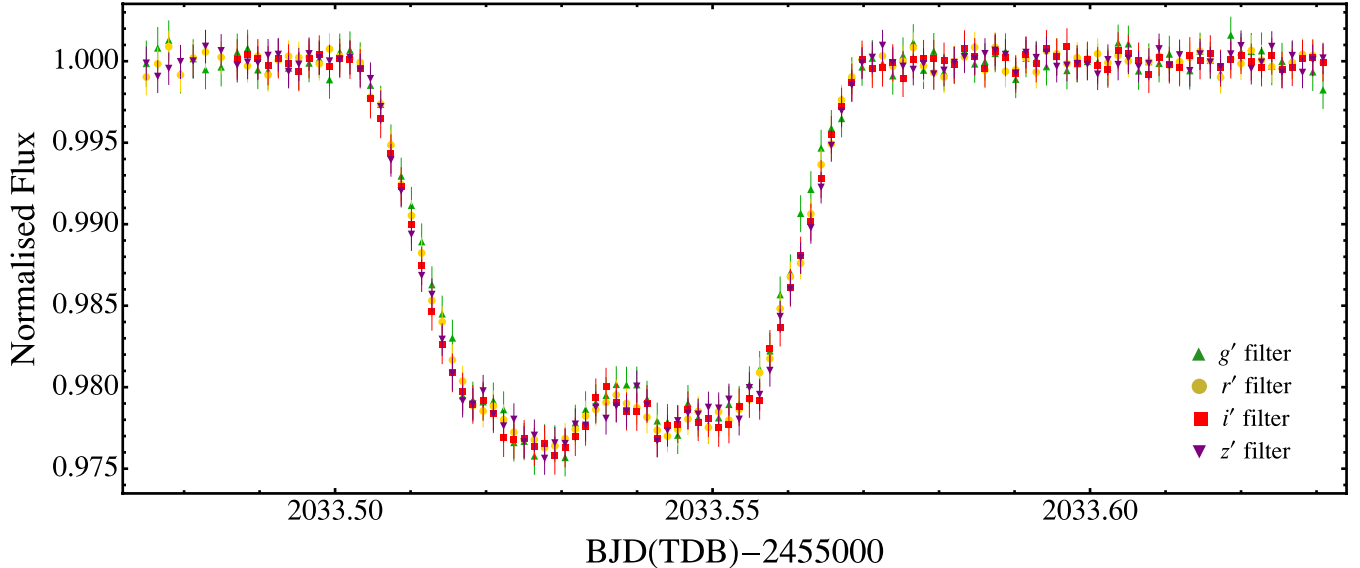
Figure 6. Superimposed optical light curves of WASP-19 obtained with GROND. Green triangles are for the data taken in the g' band, yellow dots for r', red squares for i' and purple inverted triangles for z'. The bump observed near the centre is due to the occultation of a starspot by the planet.

Southworth et al. 2012c and references therein). Briefly, we used the photometric parameters r_A, r_b and i (Section 3), published spectroscopic results (see Table 4), and theoretical stellar models to estimate the properties of the system. This was done for a range of ages to find the best-fitting evolutionary age of the star, and for five different sets of theoretical models (Southworth 2010) to determine the systematic error stemming from their use. The random errors in all input parameters were propagated to all output parameters using a perturbation analysis. We also used a model-independent method to estimate the physical parameters of the systems, via a calibration based on detached eclipsing binaries relating the host star's density to its radius (Enoch et al. 2010). Our implementation relies on the calibration coefficients for stars less than $3\,M_\odot$ calculated by Southworth (2011).

The individual solutions for each stellar model and for the empirical calibration method can be found in Table 8. The final set of physical properties was obtained by taking the unweighted mean of the sets of values obtained using stellar models, and are reported in Table 9. The accuracy of our final estimation of most of the parameters is better than those obtained by other authors. In particular, the radius of the planet was measured with a precision better than 2 per cent.

5 VARIATION OF PLANETARY RADIUS WITH WAVELENGTH

An interesting alternative to transmission spectroscopy in probing the atmospheres of TEPs is to study their transits with simultaneous photometry at different wavelengths. This strategy allows the radius of a TEP to be measured in multiple passbands and is not affected by temporal variability, for example starspots. The aim is to detect variations attributable to changes in opacity at different wavelengths (e.g. de Mooij et al. 2012; Southworth et al. 2012b; Mancini et al. 2013a,b; Fukui et al. 2013; Nikolov et al. 2013; Copperwheat et al. 2013).

Fortney et al. (2008) suggested the classification of hot Jupiters in two classes, pM and pL, depending to the incident stellar flux and the

expected amount of absorbing substances, such as gaseous titanium oxide (TiO) and vanadium oxide (VO), in their atmospheres. Receiving from its parent star an incident flux of 3.64×10^9 erg s^{-1} cm^{-2} (Hebb et al. 2010), WASP-19b would belong to the pM class of planets. Its atmosphere should be rich in oxidized elements, which should cause a variation of its radius by ~ 3 per cent between the wavelength ranges 350–400 nm and 500–700 nm. Such a variation would be directly measurable using GROND.

More recently, Madhusudhan (2012) proposed a new classification scheme for hydrogen-dominated exoplanetary atmospheres, which is based on both irradiation and the carbon-to-oxygen (C/O) ratio. The author distinguished four classes of atmosphere (O1, O2, C1 and C2) in this 2D space, each having distinct chemical, thermal and spectral properties. According to this scheme and to the temperature and incident flux of WASP-19b, it should be a C2 planet, which means that it has a C/O ratio ≥ 1, even if the O2 (C/O < 1) classification is not completely ruled out and was recently supported by Lendl et al. (2012).

As an additional possibility offered by the GROND data, we investigated the variations of the radius of WASP-19b in the wavelength ranges accessible to the instrument and compared our results with those available in the literature. For the optical passbands, we used the values of the planet/star radius reported in Table 5. The precision of the data in the NIR bands is significantly worse than in the optical bands (see Fig. 3), and the radii derived from these data are quite uncertain. It is therefore not possible to fit for the starspot parameters in these bands, despite the spot having a significant effect on the measured planetary radius. A simple fit of the NIR light curve with JKTEBOP returned transit depths which are much lower than those measured in the optical cases. This is in agreement with Ballerini et al. (2012), who showed that the presence of starspots affects the inclination and a/R_A values by up to 3σ. We therefore analysed the J, H and K data sets with PRISM+GEMC, constraining the system and the starspot parameters (size and position) to the values determined for the optical case. Since the amplitude of the anomaly is expected to decrease continually through the optical and NIR ranges, we also constrained the fitting code to explore values of

Table 3. Times of minimum light of WASP-19 and their residuals versus the ephemeris derived in this work.

Time of minimum (BJD(TDB) − 240 0000)	Cycle number	Residual (JD)	Reference
54775.33720 ± 0.00150	0	−0.000606	Hebb et al. (2010)
54776.91566 ± 0.00019	2	0.000178	Anderson et al. (2010)
54817.14633 ± 0.00021	53	0.000046	Lendl et al. (2012)
55199.73343 ± 0.00083	538	0.000134	Tifner F. (TRESCA)
55251.79657 ± 0.00014	604	−0.000113	Tregloan-Reed et al. (2013)
55252.58544 ± 0.00010	605	−0.000082	Tregloan-Reed et al. (2013)
55255.74077 ± 0.00012	609	−0.000109	Tregloan-Reed et al. (2013)
55259.68448 ± 0.00033	614	−0.000595	Colque J. (TRESCA)
55273.88282 ± 0.00062	632	−0.001360	Evans P. (TRESCA)
55299.12768 ± 0.00055	664	0.000645	Curtis I. (TRESCA)
55334.62540 ± 0.00021	709	0.000604	This work (DFOSC)
55338.56927 ± 0.00023	714	0.000275	Lendl et al. (2012)
55353.55659 ± 0.00024	733	−0.000347	This work (DFOSC)
55363.81131 ± 0.00041	746	−0.000539	Milne G. (TRESCA)
55368.54285 ± 0.00212	752	−0.002032	This work (DFOSC)
55539.72327 ± 0.00030	969	0.000279	Lendl et al. (2012)
55569.69826 ± 0.00036	1007	−0.000620	Lendl et al. (2012)
55583.10979 ± 0.00089	1024	0.000643	Curtis I. (TRESCA)
55584.68693 ± 0.00024	1026	0.000015	Lendl et al. (2012)
55584.68684 ± 0.00019	1026	0.000105	Lendl et al. (2012)
55594.15188 ± 0.00168	1038	−0.001018	This work (PEST)
55601.25164 ± 0.00071	1047	−0.000813	This work (PEST)
55602.83138 ± 0.00046	1049	0.001253	Lendl et al. (2012)
55605.19414 ± 0.00180	1052	−0.002500	This work (PEST)
55606.77464 ± 0.00022	1054	0.000317	Lendl et al. (2012)
55607.56241 ± 0.00033	1055	−0.000752	Lendl et al. (2012)
55622.55057 ± 0.00026	1074	−0.000537	Lendl et al. (2012)
55624.12787 ± 0.00142	1076	−0.000912	This work (PEST)
55632.80612 ± 0.00025	1087	0.000103	Lendl et al. (2012)
55655.68222 ± 0.00045	1116	−0.000133	Lendl et al. (2012)
55670.66976 ± 0.00064	1135	−0.000538	Lendl et al. (2012)
55677.77038 ± 0.00195	1144	0.000531	This work (PEST)
55688.81201 ± 0.00333	1158	−0.001592	Tregloan-Reed et al. (2013)
55689.60276 ± 0.00030	1159	0.000324	This work (DFOSC)
55692.75674 ± 0.00255	1163	−0.001054	This work (PEST)
55693.54639 ± 0.00013	1164	−0.000245	This work (DFOSC)
55703.79933 ± 0.00411	1177	−0.002214	This work (PEST)
55704.59078 ± 0.00034	1178	0.000396	This work (DFOSC)
55708.53495 ± 0.00015	1183	0.000374	This work (DFOSC)
55886.81234 ± 0.00208	1409	0.000100	This work (PEST)
55896.27611 ± 0.00210	1421	−0.002195	This work (PEST)
55915.20980 ± 0.00065	1445	−0.000646	This work (PEST)
55919.15485 ± 0.00103	1450	0.000200	This work (PEST)
55922.30966 ± 0.00555	1454	−0.000343	This work (PEST)
55999.61630 ± 0.00007	1552	0.000057	Bean et al. (2013)
56021.70374 ± 0.00009	1580	0.000002	Bean et al. (2013)
56029.59250 ± 0.00035	1590	0.000366	Lendl et al. (2012)
56033.53645 ± 0.00014	1595	0.000097	This work (GROND *g*)
56033.53651 ± 0.00007	1595	0.000122	This work (GROND *r*)
56033.53643 ± 0.00007	1595	0.000180	This work (GROND *i*)
56033.53652 ± 0.00009	1595	0.000187	This work (GROND *z*)
56063.51174 ± 0.00030	1633	−0.000480	Lendl et al. (2012)
56334.87208 ± 0.00053	1977	−0.000823	Evans P. (TRESCA)

the starspot contrast >0.7. With this procedure we were able to fit the NIR light curves obtaining quite realistic transit depths. These are exhibited in Fig. 10 together with the optical ones reported in Table 5, and those measured by Lendl et al. (2012), Bean et al. (2013), Anderson et al. (2010) and Tregloan-Reed et al. (2013). The vertical bars represent the relative errors in the measurements and the horizontal bars show the FWHM transmission of the passbands used. The GROND filter transmission curves are also plotted at the

base of each panel. A variation of the radius of WASP-19b along the five passbands is quite noticeable in Fig. 10.

We examined this variation with the aid of 1D model atmospheres developed in Fortney et al. (2005, 2008, 2010). By using the chemical equilibrium abundances of Lodders & Fegley (2002) at solar metallicity, and the opacity data base described in Freedman, Marley & Lodders (2008), we derived pressure–temperature (PT) profiles which are intermediate between planet-wide and dayside; they are profiles that assume 20 per cent of energy is lost to the night side (for a planet-wide profile this number is 50 per cent, whereas for a dayside this number is set to 0 per cent). We examined both the cases in which the opacity of TiO and VO molecules is excluded or included (Fig. 10 top and bottom panels, respectively). Coloured open boxes indicate the predicted values for these models integrated over the passbands of the GROND observations. Models without TiO and VO have optical transmission spectra that are dominated by Rayleigh scattering in the blue, and pressure-broadened neutral atomic lines of sodium (Na) and potassium (K) at 589 nm and 770 nm, respectively. Models with TiO and VO absorption show significant optical absorption that broadly peaks around 700 nm, with a sharp fall-off in the blue, and a shallower fall-off in the red.

Comparing the two panels of Fig. 10, it is readily apparent that the model that gives the best match to all the observational data is the one without TiO and VO opacity in the atmosphere of WASP-19b. In fact, even though both models match the optical data quite well, the presence of strong absorbers in the planetary atmosphere is not in agreement with the observational results in the NIR wavelengths. Only the model in which we neglected the presence of the two oxidized elements succeeds to explain the optical and NIR data at the same time. In particular the absorption features between 1200 and 1700 nm are quite well recovered.

6 SECONDARY-ECLIPSE ANALYSIS

We fitted the occultation light curves with a model composed of two components:

$$F(\text{mod}) = E(T_{\text{mid}}, F_{\text{p}}/F_*)B(x, y, t, z). \tag{1}$$

The first component $E(T_{\text{mid}}, F_{\text{p}}/F_*)$ is the real occultation signal, which utilizes the theoretical formulae of Mandel & Agol (2002) for a uniform source:

$$E(T_{\text{mid}}, F_{\text{p}}/F_*) = 1 - \frac{\lambda_e}{1 + 1/(F_{\text{p}}/F_*)}, \tag{2}$$

where λ_e refers to their equation (1), and mid-eclipse time T_{mid} and planet-to-star flux ratio F_{p}/F_* are set as free parameters. The second component is the baseline correction function $B(x, y, t, z)$, which is used to correct the instrumental systematics, consisting of the star position on the detector (x, y), time (t) and airmass (z) in various combinations. We find the best-fitting parameters by minimizing χ^2:

$$\chi^2 = \sum_{i=1}^{N} \frac{[F_i(\text{obs}) - F_i(\text{mod})]^2}{\sigma_{F,i}^2(\text{obs})}. \tag{3}$$

We selected the best baseline model for each night by comparing the Bayesian Information Criterion (BICs, Schwarz 1978) among different models: $BIC = \chi^2 + k \log(N)$.

We employed the Markov Chain Monte Carlo (MCMC) technique with Metropolis-Hastings algorithm and Gibbs sampling to determine the posterior probability distribution function (PDF) for each parameter. At each step, we first divided the theoretical model
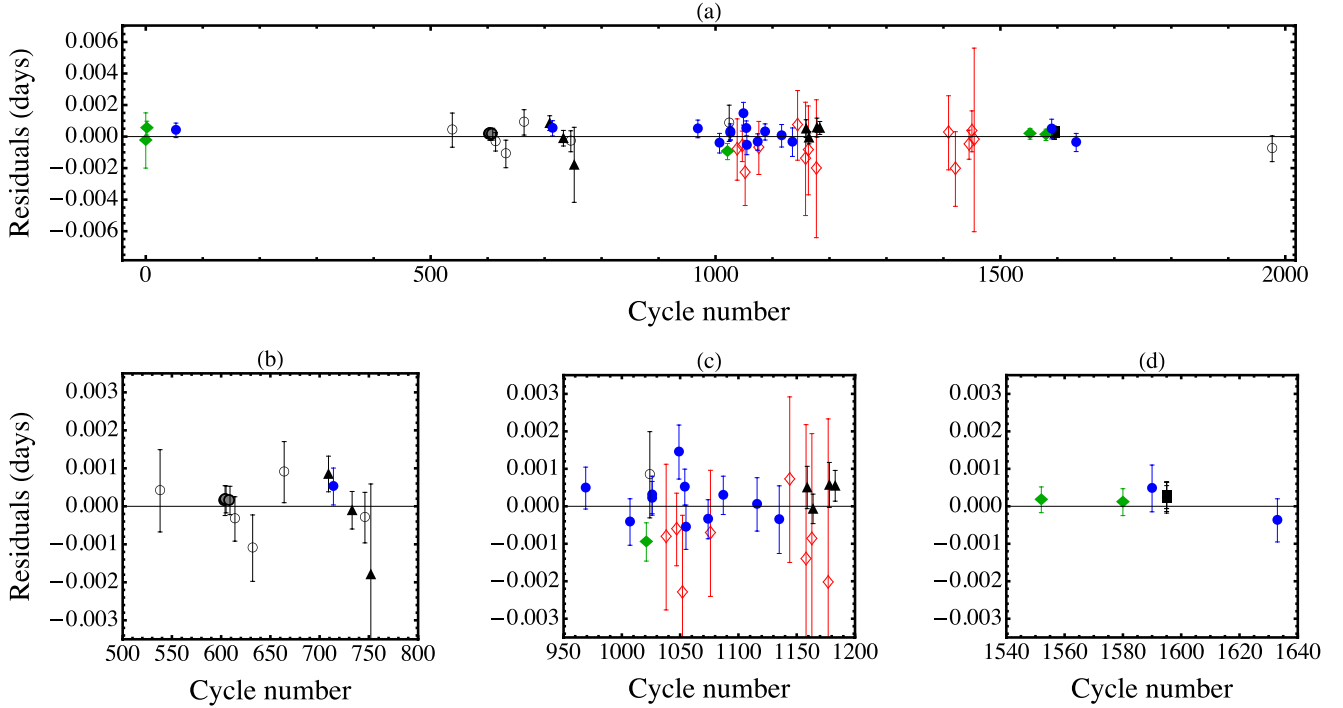
Figure 7. Panel (a): plot of the residuals of the timings of mid-transit of WASP-19 versus a linear ephemeris. The timings plotted with black triangles are from DFOSC (this work), red open diamonds from PEST (this work), black boxes from GROND (this work), blue circles from Lendl et al. (2012), grey circles from (Tregloan-Reed et al. 2013), black open circles from ETD, and green diamonds show literature values (see Table 3). Panels (b), (c) and (d): zooms in to the best-sampled regions.

Table 4. Spectroscopic properties of the host star in WASP-19 adopted from the literature and used in the determination of the LD coefficients and the physical properties of the system.

Source	WASP-19	Ref.
$T_{\rm eff}$ (K)	5460 ± 90	Doyle et al. (2013)
$[\frac{\rm Fe}{\rm H}]$ (dex)	0.14 ± 0.11	Doyle et al. (2013)
$\log g_A$ (cgs)	4.432 ± 0.013	Hellier et al. (2011)
K_A (m s^{-1})	257 ± 3	Hellier et al. (2011)

$E(T_{\rm mid}, F_{\rm p}/F_*)$ out, and then solved the baseline function coefficients using singular value decomposition (SVD, Press et al. 1992). This ensures the propagation of uncertainties from the chosen baseline function to the final PDFs. A detailed description of our MCMC process can be found in Chen et al. (2013, in preparation).

We fitted the light curves of four nights simultaneously. In this joint fit, they shared the same $T_{\rm mid}$ (phase-folded) and $F_{\rm p}/F_*$, but they were allowed to have different baselines and coefficients. The planetary-system parameters were obtained from Tables 5 and 9. The period and mid-transit times were those estimated in Section 3.1. We first ran five chains of 10^5 links to find the red noise re-scaling factor β and enlarged the flux uncertainties by this factor. Then we ran another five chains of 10^6 links to find the final PDFs. The results are listed in Table 10, while the coefficients of chosen baseline function are listed in Table 11. In Fig. 5 we show the four raw light curves, as well as the baseline-corrected phase-folded light curves. Fig. 11 shows the joint PDF between $T_{\rm mid}$ and $F_{\rm p}/F_*$.

We have found a flux ratio of 0.048 ± 0.013 per cent in the Gunn i band, which corresponds to a brightness temperature of $T_{\rm B} = 2544^{+96}_{-110}$ K. In the calculation of brightness temperature, we assumed blackbody emission for the planet and adopted the Kurucz stellar template model for the host star. The latter was interpolated using the $T_{\rm eff}$ and $[\frac{\rm Fe}{\rm H}]$ from (Doyle et al. 2013), and the $\log g_*$ obtained from this work. This brightness temperature indicates that the day-night energy redistribution efficiency is low ($\lesssim 25$ per cent). As a matter of fact, it is consistent with that derived from z'-band (Burton et al. 2012), 1.19 μm narrow band (Lendl et al. 2012), NIR bands (Anderson et al. 2010), and 2.09 μm narrow band (Gibson et al. 2010), see Fig. 12. The only exception is the other z'-band detection obtained by Lendl et al. (2012). It is also important to note that the ground-based NIR spectroscopic study on the occultations of WASP-19b by Bean et al. (2013) shows that it is cooler (~ 2250 K) than previously determined by Anderson et al. (2010) and Burton et al. (2012).

Fig. 12 shows a comparison among different dayside emission model spectra used to interpret the experimental data. The top panels are models based on the methods of Fortney et al. (2008), while bottom panels are from the literature. In particular, the top right panel shows a model with TiO in the atmosphere of WASP-19b, while the model in the top left panel has no TiO. The insets in the two top panels show the corresponding PT profiles. Both models have $T_{\rm eff} = 2525$ K, a high value that is attained by allowing no loss of absorbed energy to the night side. Therefore both of these profiles are modestly warmer than those used for modelling the transmission spectrum. The bottom panels of Fig. 12 show other models found in the literature. Specifically, the bottom-left panel shows in green an O-dominated (C/O = 0.4) model, and in red a

Table 5. Parameters of the fits to the light curves of WASP-19 from the PRISM+GEMC (GROND data) and JKTEBOP (DFOSC and PEST data) analyses. The complementary results from Tregloan-Reed et al. (2013) are labelled NTT. The final parameters are given in bold and the parameters found by other studies are also shown at the base of the table for comparison. Quantities without quoted uncertainties were not given by those authors but have been calculated from other parameters which were.

Source	Filter	$r_A + r_b$	k	i (°)	r_A	r_b
GROND	g'	0.33106 ± 0.00085	0.14206 ± 0.00038	78.39 ± 0.42	0.28987 ± 0.00076	0.04118 ± 0.00014
GROND	r'	0.33437 ± 0.00374	0.14372 ± 0.00056	78.37 ± 0.28	0.29238 ± 0.00332	0.04202 ± 0.00050
GROND	i'	0.32958 ± 0.00450	0.14386 ± 0.00080	78.98 ± 0.36	0.28822 ± 0.00388	0.04146 ± 0.00059
GROND	z'	0.32983 ± 0.00410	0.14207 ± 0.00058	78.95 ± 0.31	0.28883 ± 0.00360	0.04103 ± 0.00053
DFOSC[a]	R	0.32096 ± 0.00843	0.14028 ± 0.00121	79.40 ± 0.77	0.28148 ± 0.00717	0.03949 ± 0.00130
PEST[b]	R	0.34401 ± 0.01809	0.14722 ± 0.00270	77.42 ± 1.31	0.29986 ± 0.01525	0.04415 ± 0.00287
NTT[c]	r	0.33010 ± 0.00190	0.14280 ± 0.00060	78.94 ± 0.23	0.28884 ± 0.00165	0.04125 ± 0.00028
Final results		$\mathbf{0.33091 \pm 0.00074}$	$\mathbf{0.14259 \pm 0.00023}$	$\mathbf{78.76 \pm 0.13}$	$\mathbf{0.28968 \pm 0.00065}$	$\mathbf{0.04124 \pm 0.00012}$
Tregloan-Reed et al. (2013)		0.3301 ± 0.0019	0.1428 ± 0.0006	78.94 ± 0.23	0.2888	0.04125
Lendl et al. (2012)		0.3193	0.1423	79.54 ± 0.33	0.2796	0.0398
Bean et al. (2013)			0.0207	78.73 ± 0.20		
Abe et al. (2013)			0.141 ± 0.001	79.6 ± 0.3		

[a]The results in this row come from the analysis of eight light curves combined by phase-binning.
[b]The results in this row come from the analysis of 14 light curves combined by phase-binning.
[c]The results in this row come from the analysis of three NTT light curves performed by Tregloan-Reed et al. (2013).

Table 6. Starspot parameters derived from the PRISM+GEMC fitting of the optical GROND transit light curves for a common starspot position ($\theta = 3°36$, $\phi = 59°98$).

Parameter	Symbol	g'	r'	i'	z'
Starspot angular radius (°)	r_{spot}	9.37 ± 0.45	9.65 ± 0.50	10.50 ± 0.67	8.60 ± 0.57
Starspot contrast	ρ_{spot}	0.347 ± 0.050	0.590 ± 0.037	0.638 ± 0.020	0.618 ± 0.040
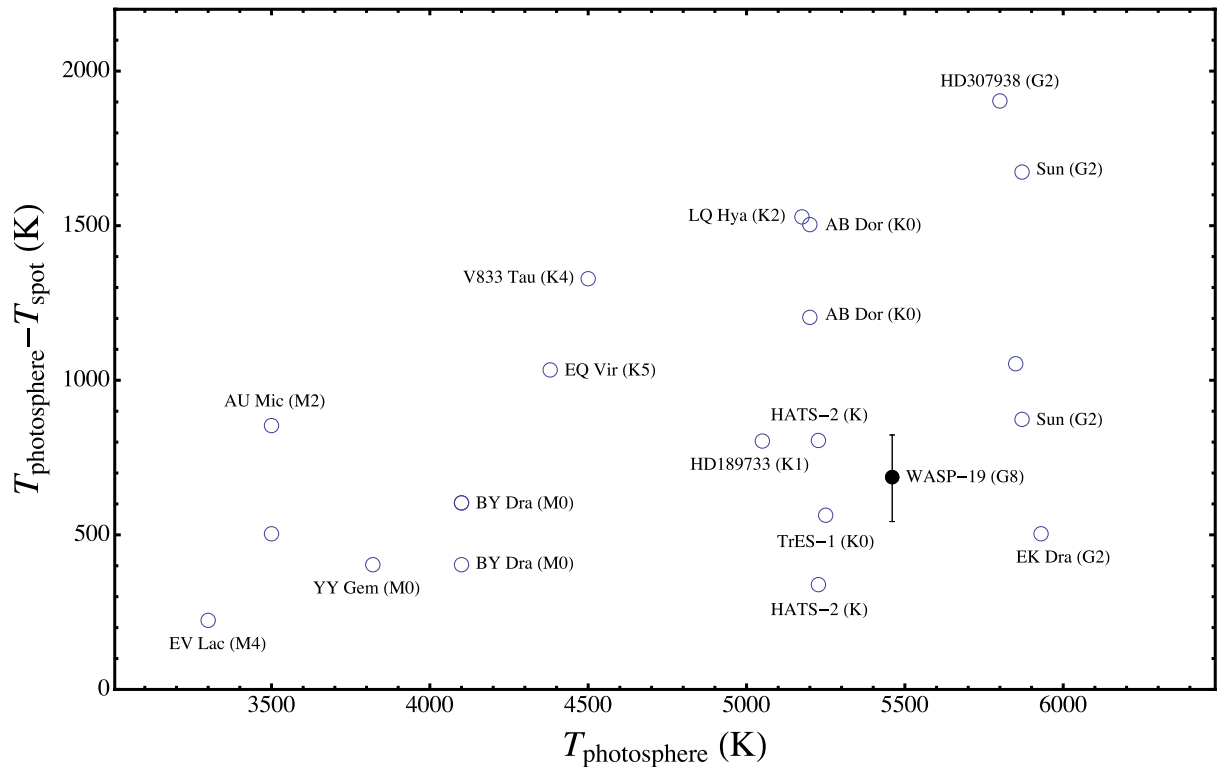
Figure 8. Spot temperature contrast with respect to the photospheric temperature in several dwarf stars taken from Berdyugina (2005). The name of the star and its spectral type are also reported for most of them. The values for TrES-1, HD189733 and HATS-2 are taken from Rabus et al. (2009), Sing et al. (2011) and Mohler-Fischer et al. (2013), respectively. The black dot refers to WASP-19 (this work). Note that some stars appear twice.
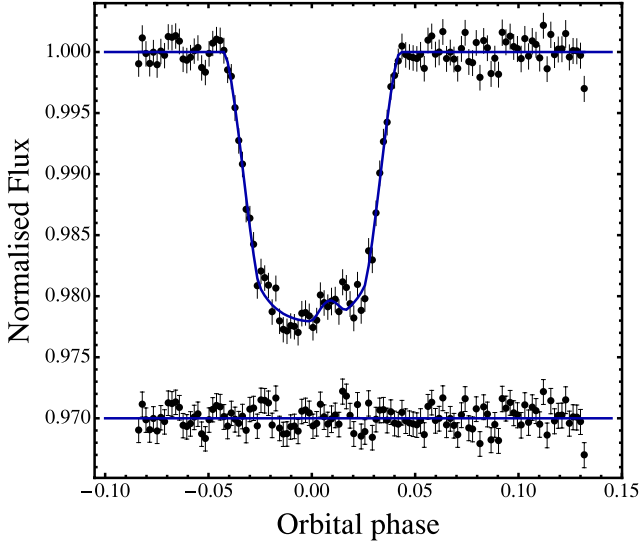
Figure 9. Transit light curve of WASP-19 observed with the Danish 1.54-m telescope on 2011/05/11. The best-fitting line has been calculated by using PRISM+GEMC codes and is compatible with the presence of a starspot.

carbon-dominated (C/O = 1.1) model (Madhusudhan 2012). Quite similar models (C/O = 0.5 and 1.0) are plotted in the bottom right panel (Bean et al. 2013).

From an inspection of the four panels, it seems that none of the models are able to explain all the data simultaneously, particularly in the NIR where there is tension between data sets. This is not necessarily surprising since they were taken by different instruments at different times. Since WASP-19 A is an active star, this indicates that it is important to do long-term monitoring of the stellar activity. Nonetheless, whilst the model with TiO (top-right panel of Fig. 12) and those from the literature (bottom panels) seem to either fit in the *Spitzer* Infrared Array Camera (IRAC) bands, or in the NIR, but not both, the model with no temperature inversion and $T_{eff} = 2525$ K

(top left panel) is the one which fits well all the IRAC data, the Bean et al. (2013) data and all data blueward of 1.2 μm, with the only exception of that measured by Lendl et al. (2012) at 0.9 μm. We therefore tentatively favour an atmosphere model that lacks a temperature inversion and has a C/O ratio that is not dramatically different from the solar value. A consistent picture from transit and secondary-eclipse data is that of a hot dayside atmosphere that lacks at strong optical absorber to drive a temperature inversion.

7 SUMMARY AND CONCLUSIONS

We have reported new broad-band photometric observations of 23 transits and four occultations in the WASP-19 planetary system. It was monitored eight times with the 1.54-m Danish telescope and 14 times with the PEST telescope in 2011 and 2012. The transit of 2012/04/15 was obtained with GROND in seven optical-IR pass-bands simultaneously, covering the wavelength range 370–2350 nm. The use of telescope defocusing resulted in light curves with scatters around the best-fitting model as low as 0.52 mmag. The GROND data show an anomaly due to the occultation of a starspot by the planet.

We modelled the Danish and PEST light curves using the JKTEBOP code. The GROND light curves were fitted using the PRISM+GEMC codes as these were designed to model starspot anomalies. Our principal results are as follows.

(i) The position and the angular dimensions of the starspot in the GROND optical light curves are in agreement with the starspot found by Tregloan-Reed et al. (2013) in a transit event observed in 2010 February.

(ii) We detected a variation of the starspot contrast as a function of the wavelength, as expected due to the different T_{eff}s of the spot and the surrounding photosphere.

(iii) The multi-colour data allowed the temperature of the starspot to be constrained to be $T_{spot} = 4777 \pm 50$ K, a value which is in agreement with those found for other similar stars (Fig. 8).

(iv) We used our data and those collected from the literature and the web archives to investigate possible transit timing variations,

Table 7. Parameters of the fit to the light curve of WASP-19, observed with the Danish 1.54-m telescope on 2011/05/11, from the JKTEBOP and PRISM+GEMC analysis.

Source	Code	$r_A + r_b$	k	i (°)	θ	ϕ	r_{spot}	ρ_{spot}
DFOSC	JKTEBOP	0.3194 ± 0.0060	0.13774 ± 0.00097	79.38 ± 0.95				
DFOSC	PRISM+GEMC	0.3250 ± 0.0087	0.13817 ± 0.00107	79.09 ± 0.67	11.35 ± 0.89	59.11 ± 5.49	6.71 ± 0.72	0.66 ± 0.06

Table 8. Derived physical properties of the WASP-19 planetary system.

	This work (dEB constraint)	This work (Claret models)	This work (Y^2 models)	This work (Teramo models)	This work (VRSS models)	This work (DSEP models)
K_b (km s^{-1})	230.3 ± 6.1	222.4 ± 3.1	222.7 ± 3.2	219.6 ± 2.4	218.8 ± 2.2	220.4 ± 2.2
M_A (M$_\odot$)	1.060 ± 0.085	0.955 ± 0.040	0.960 ± 0.041	0.920 ± 0.030	0.910 ± 0.027	0.929 ± 0.028
R_A (R$_\odot$)	1.062 ± 0.028	1.025 ± 0.014	1.027 ± 0.015	1.013 ± 0.011	1.009 ± 0.011	1.016 ± 0.010
$\log g_A$ (cgs)	4.4118 ± 0.0117	4.3966 ± 0.0064	4.3973 ± 0.0066	4.3912 ± 0.0052	4.3896 ± 0.0046	4.3927 ± 0.0048
M_b (M$_{Jup}$)	1.239 ± 0.067	1.156 ± 0.035	1.160 ± 0.036	1.128 ± 0.028	1.119 ± 0.027	1.135 ± 0.026
R_b (R$_{Jup}$)	1.471 ± 0.040	1.421 ± 0.021	1.423 ± 0.021	1.403 ± 0.016	1.398 ± 0.015	1.408 ± 0.015
ρ_b (ρ_{Jup})	0.3643 ± 0.0115	0.3772 ± 0.0083	0.3766 ± 0.0084	0.3819 ± 0.0078	0.3834 ± 0.0078	0.3806 ± 0.0075
Θ	0.02706 ± 0.00079	0.02802 ± 0.00052	0.02798 ± 0.00053	0.02838 ± 0.00047	0.02848 ± 0.00047	0.02828 ± 0.00045
a (au)	0.01704 ± 0.00045	0.01646 ± 0.00023	0.01649 ± 0.00024	0.01626 ± 0.00018	0.01620 ± 0.00016	0.01631 ± 0.00016
Age (Gyr)		$9.8^{+2.6}_{-1.9}$	$8.0^{+2.1}_{-1.5}$	$11.6^{+2.1}_{-2.0}$	$11.7^{+0.9}_{-3.0}$	$10.0^{+2.4}_{-1.2}$

Table 9. Final physical properties of the WASP-19 system, compared with results from the literature. Separate statistical and systematic error bars are given for the results from the current work.

	This work	Hebb et al. (2010)	Hellier et al. (2011)	Tregloan-Reed et al. (2013)	Lendl et al. (2012)
M_A ($M_\odot$)	$0.935 \pm 0.033 \pm 0.025$	$0.96^{+0.09}_{-0.10}$	0.97 ± 0.02	0.904 ± 0.040	$0.968^{+0.084}_{-0.079}$
R_A ($R_\odot$)	$1.018 \pm 0.012 \pm 0.009$	$0.94^{+0.04}_{-0.04}$	0.99 ± 0.02	1.004 ± 0.016	1.004 ± 0.016
$\log g_A$ (cgs)	$4.3932 \pm 0.0054 \pm 0.0039$	$4.47^{+0.03}_{-0.03}$	4.432 ± 0.013	4.391 ± 0.008	
ρ_A ($\rho_\odot$)	0.8853 ± 0.0060	$1.13^{+0.09}_{-0.09}$	$0.993^{+0.047}_{-0.042}$	$0.893 \pm .015$	$0.983^{+0.039}_{-0.036}$
M_b (M_{Jup})	$1.139 \pm 0.030 \pm 0.020$	$1.15^{+0.08}_{-0.08}$	1.168 ± 0.023	1.114 ± 0.036	1.165 ± 0.068
R_b (R_{Jup})	$1.410 \pm 0.017 \pm 0.013$	$1.31^{+0.06}_{-0.06}$	1.386 ± 0.032	1.395 ± 0.023	1.376 ± 0.046
g_b (m s^{-2})	14.21 ± 0.18	$15.5^{+1.1}_{-1.1}$	13.90 ± 0.68	14.19 ± 0.26	15.28 ± 0.053
ρ_b (ρ_{Jup})	$0.3800 \pm 0.0071 \pm 0.0034$	$0.51^{+0.06}_{-0.05}$	0.438 ± 0.028	0.384 ± 0.011	$0.447^{+0.027}_{-0.025}$
T'_{eq} (K)	2077 ± 34	2009^{+26}_{-26}	2050 ± 40	2067 ± 23	2058 ± 40
Θ	$0.02823 \pm 0.00048 \pm 0.00025$			0.02852 ± 0.00057	
a (au)	$0.01634 \pm 0.00019 \pm 0.00015$	$0.0165^{+0.0005}_{-0.0006}$	0.01655 ± 0.00013	0.01616 ± 0.00024	0.01653 ± 0.00046
Age (Gyr)	$10.2^{+2.6}_{-3.1}{}^{+1.4}_{-2.2}$	$5.5^{+9.0}_{-4.5}$		$11.5^{+2.7}_{-2.3}$	
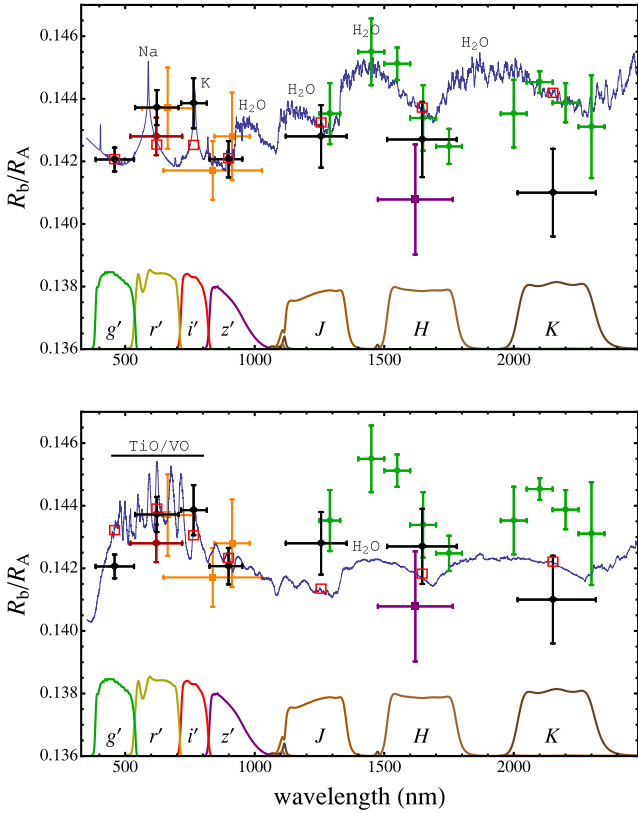
Figure 10. Variation of the planetary radius, in terms of planet/star radius ratio, with wavelength. Black diamonds are from GROND (this work), red diamond from Tregloan-Reed et al. (2013), orange boxes from Lendl et al. (2012), purple boxes from Anderson et al. (2010), green points from Bean et al. (2013). The vertical bars represent the errors in the measurements and the horizontal bars show the FWHM transmission of the passbands used. The observational points are compared with two models. These use profiles which are intermediate between planet-wide and dayside. Synthetic spectra in the top panel do not include TiO and VO opacity, while spectra in the bottom do, based on equilibrium chemistry. Red open boxes indicate the predicted values for each of the two models integrated over the passbands of the observations. Transmission curves of the GROND filters are shown at the bottom of each panel. Prominent absorption features are labelled.

Table 10. Results of the MCMC analysis of the secondary eclipses of WASP-19b.

Parameter	Units	Value
$T_{mid, occ}$	BJD$_{TDB}$	$2455721.5508^{+0.0028}_{-0.0031}$
$\phi_{mid, occ}$[a]	...	$0.5002^{+0.0036}_{-0.0039}$
T_{offset}[a]	Minutes	$0.52^{+4.0}_{-4.5}$
F_p/F_*	per cent	$0.048^{+0.013}_{-0.013}$
T_B	K	2544^{+96}_{-110}

[a]Light travel time ($\sim$16.5 s) in the system has been corrected.

but we did not find any evidence of a departure from a linear ephemeris.

(v) We used the DFOSC, PEST and GROND data sets to revise the physical parameters of the system. In particular, we obtained an estimation of the radius of WASP-19b with a precision better than 2 per cent, which reveals that the planet is larger ($R_b = 1.410 \pm 0.017$) than reported in the discovery paper and in other studies (see Table 9). This implies that the density of WASP-19b is lower than originally thought.

(vi) A joint analysis of our new photometric data and spectroscopic results from the literature supports the picture that the WASP-19 system is roughly two times older than was originally estimated by Hebb et al. (2010), in agreement with the more recent estimate of Tregloan-Reed et al. (2013).

(vii) Thanks to the ability of GROND to measure stellar flux simultaneously through seven different filters, covering quite a large range of the optical and NIR windows, we measured a radius variation of WASP-19b as a function of wavelength. We joined our measurements with those obtained by other authors to reconstruct a transmission spectrum of the planet's atmosphere in terms of planet/star radius ratio. This transmission spectrum was compared with two synthetic spectra, based on model atmosphere in chemical equilibrium, where the PT profiles are assumed intermediate between planet-wide and dayside, but with different opacity characteristics (with and without gaseous TiO and VO). We found that WASP-19b's atmosphere is presumably dominated by absorption by H_2O, Na and K, and no evidence for a strong optical absorber at

Table 11. Coefficients for adopted baseline function.

Coeff.	2010-05-24[a]	2011-05-14[b]	2011-05-25[c]	2011-06-09[d]
c_0	$1.000199 \, ^{+0.000045}_{-0.000046}$	$1.000364 \, ^{+0.000060}_{-0.000061}$	$1.000117 \, ^{+0.000079}_{-0.000080}$	$0.999764 \, ^{+0.000076}_{-0.000077}$
c_1	$-0.002373 \, ^{+0.000089}_{-0.000091}$	$-0.001064 \, ^{+0.000098}_{-0.000097}$	$-0.001091 \, ^{+0.000032}_{-0.000032}$	$-0.00193 \, ^{+0.00019}_{-0.00018}$
c_2	...	...	$0.0456 \, ^{+0.0039}_{-0.0039}$	$0.001649 \, ^{+0.000071}_{-0.000070}$
c_3	...	...	$-0.00315 \, ^{+0.00059}_{-0.00059}$	$0.00216 \, ^{+0.00022}_{-0.00022}$
c_4	...	...	...	$0.001203 \, ^{+0.000039}_{-0.000037}$
c_5	...	...	...	$0.0357 \, ^{+0.0013}_{-0.0014}$

Note: [a]$B = c_0 + c_1 z$; [b]$B = c_0 + c_1 x$; [c]$B = c_0 + c_1 x + c_2 t + c_3 z$; [d]$B = c_0 + c_1 x + c_2 y + c_3 xy + c_4 y^2 + c_5 t$.
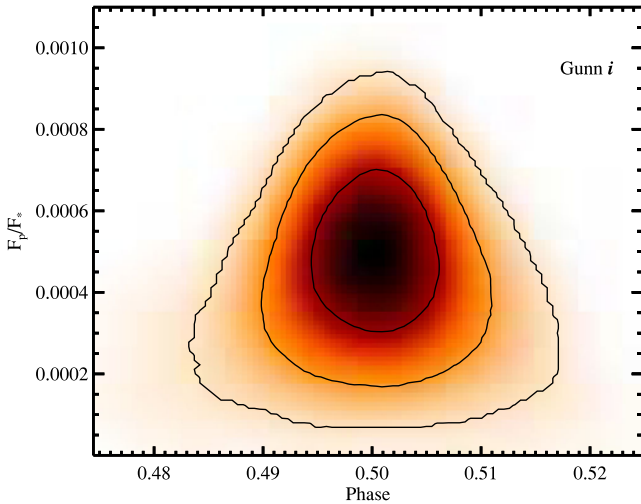
Figure 11. Correlation map between mid-eclipse time and flux ratio from the MCMC analysis. The mid-eclipse times have been converted to phases for display purpose. The contour levels indicate the 68.3 per cent (1σ), 95.4 per cent (2σ) and 99.7 per cent (3σ) confidence levels, respectively.

low pressure, which agrees well with the fact that the atmosphere lacks a dayside inversion.

(viii) A joint analysis of the four occultations of WASP-19b was performed and from this it was possible to measure an occultation depth of 0.048 ± 0.013 per cent, corresponding to an *i*-band brightness temperature of $T_B = 2544^{+96}_{-110}$ K. We combined this measurement with all others available in the literature, providing a very wide coverage of the planet's spectral energy distribution (750–8000 nm). We compared these experimental results with two dayside emission model spectra taken from the literature and another two models constructed following the methodology of Fortney et al. (2008), again considering both the cases with and without TiO in the atmosphere of WASP-19b. The model, corresponding to an atmosphere with a temperature of $T_{eff} = 2525$ K, and no temperature inversion, returned the best fit of the experimental measurements.

(ix) We conclude that WASP-19b seems to be inefficient at homogenizing temperature, given how hot the dayside is. This agrees well with the advective and radiative time-scale argument from Cowan & Agol (2011). For these very hot planets, the radiative time is short, so advection fails to move energy fast enough to homogenize the temperature.

(x) The planet probably does not fit the Fortney et al. (2008) or Madhusudhan (2012) classification schemes. It seems to be an oxygen-rich planet (C/O < 1), but with no TiO. A possible explanation is that it is cold-trapped at depth.

Figure 12. Dayside emission spectrum of WASP-19b in terms of the planet-to-star flux ratio. Our Gunn i' band detection is plotted with a purple diamond with error bars. Blue dots are previous detections in z' band and a 1.19 μm narrow band (Lendl et al. 2012). Another detection in z' band is represented by a pink dot (Burton et al. 2012). Orange dots are measurements obtained in NIR bands by Bean et al. (2013). Black diamonds are measurements realized by Anderson et al. (2010) in the H band, Gibson et al. (2010) in the 2.09 μm narrow band and Anderson et al. (2013) in the four *Spitzer* IRAC bands. Different model spectra are shown in the four panels. Top left panel: a model atmosphere with no temperature inversion and $T_{eff} = 2525$ K. Top right panel: a model with a temperature inversion and the same T_{eff}. The insets of these two panels show the corresponding PT profiles for the models. Bottom left panel: models from Madhusudhan (2012). The green line represents an oxygen-dominated (CO = 0.4) model while the red line accounts for a carbon-dominated (C/O = 1.1) model. Bottom right panel: models taken from Bean et al. (2013). The green and red lines are as for the bottom left panel, but with a slightly different composition, C/O = 0.5 and 1.0, respectively.

REFERENCES

Abe L. et al., 2013, A&A, 553, A9

Anderson D. R. et al., 2010, A&A, 513, L3

Anderson D. R. et al., 2013, MNRAS, 430, 3422

Ballerini P., Micela G., Lanza A. F., Pagano I., 2012, A&A, 539, A140

Bean J. L., Désert J.-M., Seifahrt A., Madhusudhan N., Chilingarian I., Homeier D., Szentgyorgyi A., 2013, ApJ, 771, 108

Berdyugina S. V., 2005, Living Rev. Solar Phys., 2, 8

Burton J. R., Watson C. A., Littlefair S. P., Dhillon V. S., Gibson N. P., Marsh T. R., Pollacco D., 2012, ApJS, 201, 36

Claret A., 2004, A&A, 428, 1001

Collier Cameron A., 1992, in Byrne P. B., Mullan D. J., eds, Surface Inhomogeneities on Late-type Stars. Springer, Berlin, p. 33

Copperwheat C. M. et al., 2013, preprint (arXiv:1305.4166)

Cowan N. B., Agol E., 2011, ApJ, 729, 54

de Mooij E. J. W. et al., 2012, A&A, 538, A46

Dominik M. et al., 2010, Astron. Nachr., 331, 671

Doyle A. P. et al., 2013, MNRAS, 428, 3164

Dragomir D. et al., 2011, ApJ, 142, 115

Enoch B., Collier Cameron A., Parley N. R., Hebb L., 2010, A&A, 516, A33

Fortney J. J., Marley M. S., Lodders K., Saumon D., Freedman R., 2005, ApJ, 627, L69

Fortney J. J., Lodders K., Marley M. S., Freedman R. S., 2008, ApJ, 678, 1419

Fortney J. J., Shabram M., Showman A. P., Lian Y., Freedman R. S., Marley M. S., Lewis N. K., 2010, ApJ, 709, 1396

Freedman R. S., Marley M. S., Lodders K., 2008, ApJ, 174, 513

Fukui A. et al., 2013, ApJ, 770, 95

Gibson N. P. et al., 2008, A&A, 492, 603

Gibson N. P. et al., 2010, MNRAS, 404, L114

Gillon M., Pont F., Moutou C., Bouchy F., Courbin F., Sohy S., Magain P., 2006, A&A, 459, 249

Greiner J. et al., 2008, PASP, 120, 405

Harpsøe K. B. W. et al., 2013, A&A, 549, A10

Hebb L. et al., 2010, ApJ, 708, 224

Hellier C., Anderson D. R., Collier-Cameron A., Miller G. R. M., Queloz D., Smalley B., Southworth J., Triaud A. H. M. J., 2011, ApJ, 730, L31

Lendl M., Gillon M., Queloz D., Alonso R., Fumel A., Jehin E., Naef D., 2013, A&A, 552, A2

Lodders K., Fegley B., 2002, Icarus, 155, 393

Madhusudhan N., 2012, ApJ, 758, 36

Mancini L. et al., 2013a, A&A, 551, A11

Mancini L. et al., 2013b, MNRAS, 430, 2932

Mandel K., Agol E., 2002, ApJ, 580, L171

Mohler-Fischer M. et al., 2013, A&A, preprint (arXiv:1304.2140)

Nikolov N., Henning Th., Koppenhoefer J., Lendl M., Maciejewski G., Greiner J., 2012, A&A, 539, 159

Nikolov N., Chen G., Fortney J., Mancini L., Southworth J., van Boekel R., Henning Th., 2013, A&A, 553, A26

Pierini D. et al., 2012, A&A, 540, A45

Press W. H., Teukolsky S. A., Vetterling W. T., Flannery B. P., 1982, Numerical Recipes in FORTRAN. Cambridge Univ. Press, Cambridge

Rabus M. et al., 2009, A&A, 494, 391

Sanchis-Ojeda R., Winn J. N., 2011, ApJ, 743, 61

Schwarz G. E., 1978, Ann. Stat., 6, 461

Silva A. V. R., 2003, ApJ, 585, L147

Sing D. K. et al., 2011, MNRAS, 416, 1443

Southworh J., 2008, MNRAS, 386, 1644

Southworth J., 2010, MNRAS, 408, 1689

Southworth J., 2011, MNRAS, 417, 2166

Southworth J., 2012, MNRAS, 426, 1291

Southworth J., Maxted P. F. L., Smalley B., 2004, MNRAS, 349, 547

Southworth J. et al., 2009a, MNRAS, 396, 1023

Southworth J., Hinse T. C., Burgdorf M. et al., 2009b, MNRAS, 399, 287

Southworth J., Bruni I., Mancini L., Gregorio J., 2012a, MNRAS, 420, 2580

Southworth J., Mancini L., Maxted P. F. L., Bruni I., Tregloan-Reed J., Barbieri M., Ruocco N., Wheatley P. J., 2012b, MNRAS, 422, 3099

Southworth J. et al., 2012c, MNRAS, 426, 1338

Stetson P. B., 1987, PASP, 99, 191

Strassmeier K. G., 2009, A&AR, 17, 251

Tregloan-Reed J., Southworth J., Tappert C., 2013, MNRAS, 428, 3671

Vogt S. S., Hatzes A., Misch A., Kürster M., 1999, ApJS, 121, 547

Winn J. N. et al., 2008, ApJ, 683, 1076

This paper has been typeset from a TEX/LATEX file prepared by the author.